Materials Advances

ROYAL SOCIETY OF CHEMISTRY

PAPER

View Article Online
View Journal | View Issue

Cite this: *Mater. Adv.*, 2023, 4, 5338

Remarkably enhanced upconversion luminescence in Na^+ codoped spinel nanoparticles for photothermal cancer therapy and SPECT imaging†

Annu Balhara,[ab] Santosh K. Gupta, *[ab] Nidhi Aggarwal,[c] Swapnil Srivastava,[c] Jiban Jyoti Panda, *[c] Sourav Patra,[ad] Avik Chakraborty,[ae] Sutapa Rakshit[ae] and Rubel Chakravarty[ad]

Glioblastoma multiforme (GBM) is the most fatal brain tumor and chemo/radiotherapeutic options and other palliative care have not fetched much success in its management due to the highly heterogeneous nature of GBM tissue and the presence of the blood–brain barrier. Impressively, Na^+ co-doped $ZnAl_2O_4$:Ho^{3+}, Yb^{3+} upconversion nanoparticles (UCNPs) with remarkably enhanced upconversion luminescence (UCL) have demonstrated good cellular uptake, bio/cyto compatibility and anticancer efficacy in C6 glioma cells. The % cell viability of C6 cells treated with UCNPs decreased to 46% under 980 nm near infrared (NIR) laser exposure exhibiting an excellent potential in photothermal therapy (PTT). Laser power dependence studies explain the UC mechanism and the role of Na^+ ions in the UC luminescence enhancement is also investigated using density functional theory (DFT) calculations and positron annihilation lifetime spectroscopy (PALS). The Na^+ ion codoping resulted in a significant lowering of zinc vacancies in $ZnAl_2O_4$:Ho^{3+}, Yb^{3+}, indicating its effective role in eliminating defect-induced non-radiative channels. Intrinsically (166-Holmium) radiolabeled $ZnAl_2O_4$:Yb^{3+}, $^{166}Ho^{3+}$, Na^+ has also shown great potential towards *in vivo* single-photon emission computed tomography (SPECT) imaging. The results presented herein highlight the potential of this highly upconvertible molecule for dual modality SPECT/optical imaging for therapeutic and theranostic applications as well as for photothermal cancer therapy.

Received 7th July 2023,
Accepted 4th October 2023

DOI: 10.1039/d3ma00376k

rsc.li/materials-advances

1. Introduction

Cancer is a life-threatening malady affecting a vast number of people worldwide. According to the global statistics, cancer accounted for approximately 10 million deaths and more than 19.3 million fresh cases in the year 2020.[1] Theranostic agents are promising for modern biomedical applications as they play both diagnostic and therapeutic roles.[2,3] Luminescent nanomaterials have attracted significant attention for image-guided cancer therapy and nanomedicine based applications. In the recent past, the use of multifunctional luminescent materials as imaging probes for multiplexed imaging and photo-triggered targeted drug delivery in the tumor tissues has proved to be an area of great interest for researchers.[4] Bioimaging modalities for tumor diagnosis include optical imaging, positron emission tomography (PET), magnetic resonance imaging (MRI), computed tomography (CT), and single-photon emission computed tomography (SPECT). Moreover, combining photothermal therapy (PTT) triggering agents with multiple bioimaging modalities, such as optical imaging and SPECT/CT offers a new direction for *in vivo* theranostics.[5] Multi-modal imaging is gaining attention as it offers better imaging contrast and sensitivity for the diagnosis of tumors.[6] Anticancer agents performing bioimaging and therapeutics simultaneously are in demand for next-generation theranostics. Image-guided photothermal therapy offers potential non-invasive cancer therapeutics, but the major limitation associated with the traditional phototherapy involves the use of harmful ultraviolet (UV) light sources along with its demerit of lower tissue penetration.[7] NIR-absorbing upconversion nanoparticles (UCNPs) are endowed

[a] *Homi Bhabha National Institute, Anushaktinagar, Mumbai 400094, India. E-mail: santoshg@barc.gov.in*
[b] *Radiochemistry Division, Bhabha Atomic Research Centre, Trombay, Mumbai 400085, India*
[c] *Institute of Nano Science and Technology, Mohali, Punjab, India. E-mail: jyoti@inst.ac.in*
[d] *Radiopharmaceuticals Division, Bhabha Atomic Research Centre, Trombay, Mumbai 400085, India*
[e] *Radiation Medicine Centre, Bhabha Atomic Research Centre, Parel, Mumbai 400012, India*

† Electronic supplementary information (ESI) available. See DOI: https://doi.org/10.1039/d3ma00376k

with a remarkable tissue penetration power, and a unique capability of converting NIR to UV light in order to carry out the photoreaction necessary for its application as a theranostic agent.[8,9] UCNPs are conventionally functionalized with anticancer molecules, photothermal agents, and photo-sensitizers, which could possibly absorb the released high energy photons and produce ROS to aid in cancer cell killing. Wang and co-workers have depicted heightened *in vivo* photodynamic effect by loading a photosensitizer, Chlorin e6 (Ce6), in PEGylated UCNPs for cancer therapy.[10] In the recent past, lanthanide-doped UCNPs have emerged to be of great potential for biomedicine platforms owing to their exceptional physico-chemical and biological properties, *viz.*, higher anti-Stokes shift, longer fluorescence lifetime, high photo and chemical stability, low cytotoxicity, and lower background scattering.[11,12] Many lanthanide-doped-UCNPs are also known to convert the laser energy into thermal energy when delivered to the tumor tissues, thereby mediating the photothermal death of the tumorous tissue.[13] Tsai and co-workers demonstrated NIR-triggered phototherapeutic effects mediated by angiopep-2 functionalized UCNPs in brain glioblastoma models.[14] A plethora of UCNP-based nanosystems, such as core–shell UCNPs,[15,16] polymer-coated UCNPs,[17] SiO_2 functionalized UCNPs,[18] and metal-UCNPs,[19,20] have been primarily explored as theranostic agents in cancer.

Upconversion luminescence (UCL) in lanthanide (Ln^{3+}) doped phosphors has been thoroughly investigated by researchers and many reviews have summarized the progress made in the development of UC phosphors,[21,22] where Er^{3+}, Ho^{3+}, and Tm^{3+} doped phosphors have received more attention owing to strong UCL that could be ascribed to their ladder-like energy levels.[23] The Ho^{3+} doped materials are known for the upconversion of two or more NIR photons resulting in the red, green, and NIR emissions but display weak UCL due to spin forbidden 4f–4f transitions and the poor absorption of NIR photons.[21,23] Though the luminescence can be enhanced by increasing the doping concentrations, the rare earth ions as dopants have low-doping optimal concentrations limited by the concentration quenching observed at higher dopant concentrations.[21] Therefore, Yb^{3+} having large absorption coefficient for the NIR region is essentially codoped in Ho^{3+} doped phosphors as a sensitizer for efficient NIR pumping and energy transfer to activator Ho^{3+} ions.[23,24] Several studies have reported the boost in the UCL in different Ho^{3+}/Yb^{3+} co-doped hosts.[23–27] The rational choice of hosts also impacts the luminescence characteristics of the phosphors and a good host should satisfy particular criteria. Since halide and oxysulfide based hosts suffer from poor photostability, hygroscopicity, and toxicity, suitable oxide-based compounds are preferred and they possess superior UCL properties.[23]

Another emerging application of Ln^{3+} doped UCNPs is virus and bacterial deactivation that is triggered by effective ultraviolet-C (UV-C) emission in the effective germicidal region (220–280 nm).[28] Phosphors emitting UV-C light can be an alternative for current UV lamps (mercury lamps at 254 nm) with lower efficiency, mainly for the microbial disinfection of water. Though the UV-C upconversion is achievable by co-doping of Ho^{3+} ions, which can be attributed to their richness of intermediate energy levels, studies exploring the UV-C emission by Ho^{3+} doped phosphors are still rare. In 2010, Chen *et al.*[29] reported UV-C emission in $NaYF_4$:Yb^{3+}/Ho^{3+} powders under 970 nm excitation, but could only achieve very weak emission at 247 nm even at a high pump power of 37 W cm^{-2}, which is not suitable for practical applications.

The desired UCL intensity enhancement, controllable emission, chromaticity, and high color purity required for emerging applications could not be achieved by merely codoping Yb^{3+} ions as higher concentrations of RE^{3+} are detrimental to UCL.[30] Therefore, researchers have focussed on crystal field modulation, which is an effective way to improve upconversion emission intensity essential for practical applications.[31] The same could be achieved by codoping of non-luminous centres that play the role of local field modifiers and surface enhancers, leading to the successful increment in photoluminescence intensity. In recent years, many publications showcased the role of alkali ion (Li^+, Na^+, and K^+) and Mg^{2+} codoping in boosting the UCL and DC emission, in order to achieve tunable emission.[30–35] In the last decade, some publications have revealed the role of alkali metals in improving both UC and DC emission intensity, with majority of them focussing on Li^+ ion co-doping in different Ho^{3+} activated host matrices.[33,36] The effect of Na^+ codoping has been also explored in phosphors, thereby enhancing emission efficiency[32,34,35,37,38] but there are very few reports in the literature that emphasize the effect of Na^+ codoping in Ho^{3+}/Yb^{3+} doped materials. Among many oxide hosts activated with RE^{3+} ions, $ZnAl_2O_4$ with a cubic-type spinel lattice is a potential host due to its excellent properties like low phonon energy, non-toxicity, high photochemical and thermal stability, low cost, radiation stability, hydrophobicity, and wide band gap ($\sim$3.8 eV).[39–41] Spinels consisting of Zn^{2+} ions as RE^{3+} activated hosts (AB_2O_4:RE^{3+}) have been explored for their efficient emission properties and ability to incorporate RE^{3+} ions at tetrahedral (A^{2+}) and octahedral (B^{3+}) sites. Moreover, an enhancement in UCL was obtained in Ho^{3+}/Yb^{3+} doped spinels, by codoping of non-luminous centers as charge compensators.[42,43] To the best of our knowledge, Ho^{3+}/Yb^{3+} codoping in the zinc aluminate host and the effect of Na^+ co-doping on UCL have not been reported so far.

These favorable characteristics of the zinc aluminate spinel host and the biomedical potential of Ho^{3+} coupled with its suitable radiological half-life have pushed us to explore the potential of $ZnAl_2O_4$:Ho^{3+} sensitized with Yb^{3+} and co-doped with Na^+ for SPECT imaging-guided targeted drug or radionuclide delivery.[44–46] Radioactive labeling is considered as a fundamental phenomenon in biology-related applications. Lohar *et al.* have highlighted the potential of Ho-166 for intra-arterial radiation therapy owing to its excellent radiological properties [half-life = 26.8 h, high energy β^- emission with E_{max} $\sim$ 1.85 MeV (50.0%) and 1.74 MeV ($\sim$49%), and 80.6 keV γ-photon emission] and feasibility for its production on a large scale *via* simple ^{165}Ho (n, γ) ^{166}Ho reaction with suitable specific activity in moderate flux research nuclear reactors.[45]

The use of photoreactions to provide modulated delivery of a diagnostic or therapeutic agent to the diseased biological tissues as in cancer has been explored widely in the recent past.[7] Therefore, intrinsically radiolabelled Ho^{3+} doped UCNPs present the potential for multi-mode SPECT/optical imaging, which utilizes integrated nuclear imaging and fluorescence imaging-guided glioma therapy.

Thus, this study reports a new upconverting material $ZnAl_2O_4$:Ho^{3+}, Yb^{3+}, Na^+ and an effort was made to enhance and tune the UC emissions of Ho^{3+} ions on NIR excitation *via* codoping of Na^+ ions. The $ZnAl_2O_4$ host has been selected for the Ho^{3+}/Yb^{3+} codoping, due to its efficient photoluminescence properties. In this regard, a series of $ZnAl_2O_4$:1%Ho^{3+}, 5%Yb^{3+}, x%Na^+ (x = 0 to 10 mol %) samples were synthesized using the solid-state route. The role of Na^+ ions in boosting the visible, blue, and UV-C UC emissions was identified using the photoluminescence studies, lifetime decay measurements, PALS, and DFT studies. The mechanisms of UC processes were studied with the help of UC emission intensity dependencies on the 980 nm laser power. Additionally, herein, for the first time, we have tried to explore solely our upconverting nanomaterial (without any further down processing or with any carrier/coating) as a new-modality for glioma therapy. We investigated the *in vitro* behaviour and anticancer efficacy of our novel upconverting nanomaterial in C6 rat-glioma cells to establish it as a prospective candidate for future glioma therapy. We further explored this material for *in vivo* SPECT imaging using intrinsically radiolabeled $ZnAl_2O_4$:Yb^{3+}, $^{166}Ho^{3+}$, Na^+. Its radiochemical purity was established using thin-layer chromatography. The *in vitro* stability of intrinsically radiolabeled $ZnAl_2O_4$:$^{166}Ho^{3+}$ (^{166}Ho is a radioactive isotope) was determined under physiological conditions over a period of ~6 half-lives of ^{166}Ho. The *in vivo* stability of intrinsically radiolabeled $ZnAl_2O_4$:Yb^{3+}, $^{166}Ho^{3+}$, Na^+ was demonstrated by SPECT/CT imaging in healthy Wistar rats.

The experimental section consists of synthesis, instrumentation details, computational methodology, production of ^{166}Ho, synthesis and photothermal effect of $ZnAl_2O_4$:Yb^{3+}, Ho^{3+}, Na^+, cellular uptake studies performed in C6 cells, *in vitro* biocompatibility study performed in fibroblast cells, *in vitro* anticancer efficacy of UCNPs determined in C6 glioma cells, scratch wound healing assay, synthesis of intrinsically radiolabeled $ZnAl_2O_4$:Yb^{3+}, $^{166}Ho^{3+}$, Na^+, and preclinical studies with intrinsically radiolabeled $ZnAl_2O_4$:Yb^{3+}, $^{166}Ho^{3+}$, Na^+, which are elaborated in the ESI† as S1–S11, respectively.

2. Results and discussion

2.1. Structure and phase studies

Fig. 1(a) demonstrates the XRD patterns of doped $ZnAl_2O_4$:1%Ho^{3+} and codoped $ZnAl_2O_4$:1%Ho^{3+}, 5%Yb^{3+}, x%Na^+ (x = 0, 1, 2, 5, 7 and 10 mol%) samples. Scheme 1 demonstrates the synthesis of $ZnAl_2O_4$:Ho^{3+}, Yb^{3+}, Na^+ UCNPs by the solid-state reaction. The diffraction peaks attained in the XRD patterns can be assigned to the formation of the cubic $ZnAl_2O_4$ spinel phase in all the doped and codoped $ZnAl_2O_4$ samples (PDF card – 01-070-8182). A small peak located at a 2θ value of ~30° appears in all the Yb^{3+} codoped samples and can be attributed to Yb_2O_3 residue. Fig. 1(b) shows the crystal structure of $ZnAl_2O_4$ with Zn^{2+} ions occupying tetrahedral and Al^{3+} ions occupying octahedral sites in cubic normal spinel arrangement. The substitution of Ho^{3+} (0.901 Å) and Yb^{3+} (0.868 Å) ions having large ionic radii in Zn^{2+} (0.74 Å) sites is the likely substitution. There is a large size mismatch for Ho^{3+}, Yb^{3+} ions and Al^{3+} (0.535 Å) and substitution in Al^{3+} sites is unlikely. Due to the large ionic radius of Na^+ ions (1.02 Å), Na^+ ions also occupy Zn^{2+} sites. We synthesized a Ho^{3+} and Na^+ ion codoped Yb_2O_3 sample to investigate the contribution from Ho^{3+} ions present in the Yb_2O_3 impurity phase in the upconversion emissions. The XRD pattern for the same is provided in Fig. S1 (ESI†).

Before we move ahead and exploit the positive aspects of the dopant, sensitizer, and sodium ions, we wanted to check the feasibility of zinc aluminate spinel to successfully accommodate tri-doping species, *viz*, Ho^{3+}, Yb^{3+}, and Na^+. To explore the feasibility of formation of the tri-doped system, we have calculated defect formation energies. The details about the computational calculations are provided in Section S2.1 (ESI†). As can be seen from Table S1 (ESI†), the calculated defect formation energy for Ho^{3+} is negative (−1.20 eV), indicating that doping is thermodynamically feasible. Interestingly, the defect formation energy becomes more negative when codoped with Yb^{3+} and Na^+ (−5.51 eV). This indicates that the tri-doping is highly favoured over single element doping.

FTIR spectroscopy was performed to get an insight about the phase and local structure of $ZnAl_2O_4$. Fig. 1(c) depicts the FTIR spectrum of doped and codoped $ZnAl_2O_4$ samples and the absorption bands at 649 cm^{-1}, 547 cm^{-1}, and 474 cm^{-1} can be assigned to the symmetric stretching, symmetric bending, and asymmetric stretching modes of the AlO_6 groups, respectively.[40] The FTIR spectroscopy reveals some inversion in the $ZnAl_2O_4$ spinel structure that could be inferred from the appearance of a less intense shoulder band at ~850 cm^{-1} due to tetrahedral AlO_4 groups.[40]

2.2. Morphostructural and elemental analysis

The information regarding the morphology and mean particle size could be inferred from the FE-SEM images presented in Fig. S2 (ESI†). The particles in the doped and codoped $ZnAl_2O_4$:Ho^{3+}, Yb^{3+}, Na^+ samples have a spherical morphology and uneven particle size distribution. The EDS spectra of $ZnAl_2O_4$:1%Ho^{3+}, $ZnAl_2O_4$:1%Ho^{3+}, 5%Yb^{3+}, and $ZnAl_2O_4$:1%Ho^{3+}, 5%Yb^{3+}, 5%Na^+ samples are presented in Fig. S3 (ESI†), which clearly show the successful incorporation of Yb^{3+} and Ho^{3+} ions. The incorporation of Na^+ ions in the lattice of $ZnAl_2O_4$ was studied using laser-induced breakdown spectroscopy (LIBS) and the LIBS emission spectra clearly show the presence of Na atomic emission doublet lines at 589.995 nm and 589.592 nm (Fig. S4a, ESI†), indicating successful incorporation in the parent crystal. Further description regarding the information obtained from LIBS is provided in Section S2.4 and Fig. S4b, c

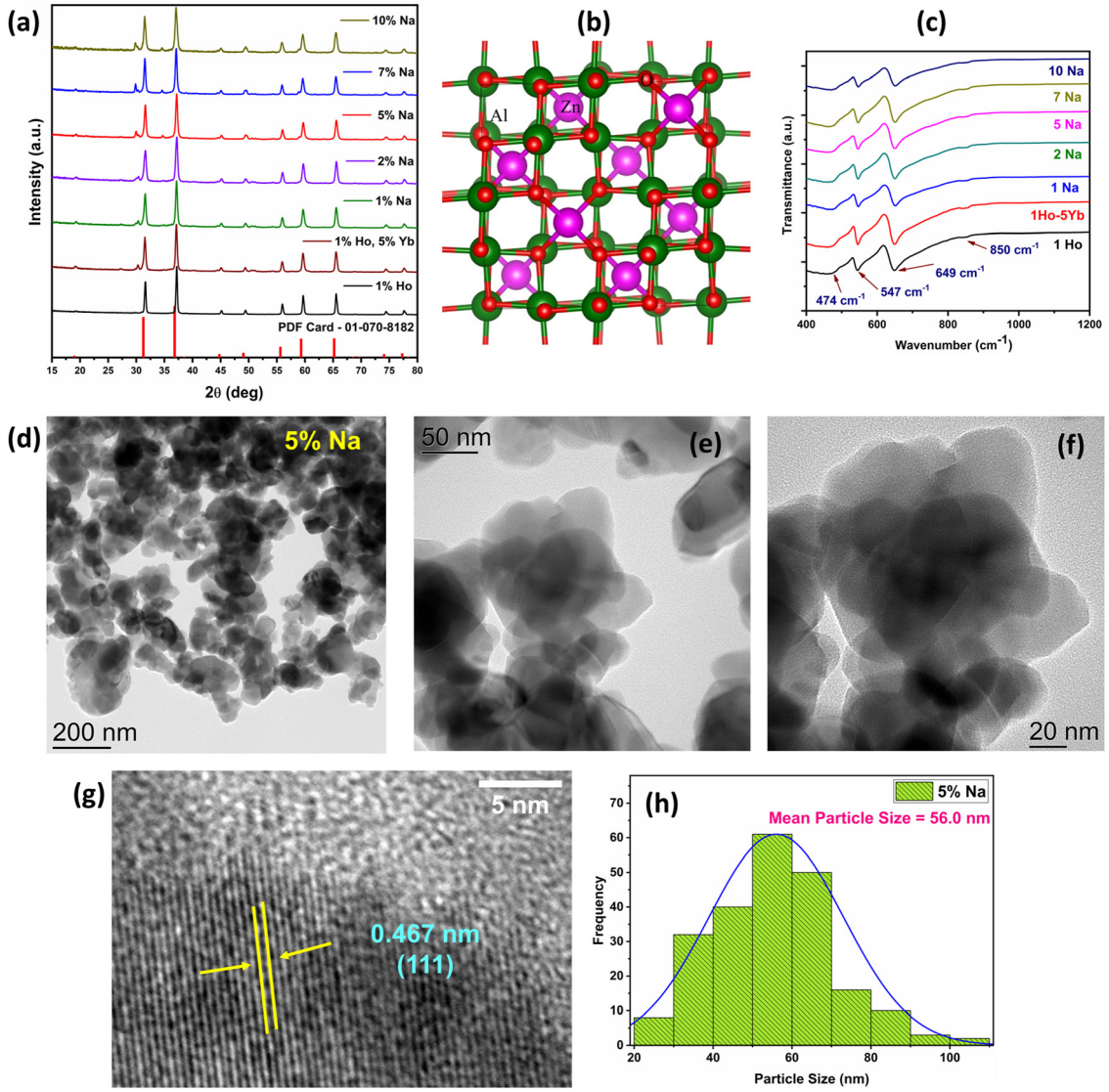

Fig. 1 (a) XRD patterns of $ZnAl_2O_4$:1%Ho^{3+} and codoped $ZnAl_2O_4$:1%Ho^{3+}, 5%Yb^{3+}, *x*%Na^+ (*x* = 0, 1, 2, 5, 7 and 10 mol%) samples; (b) crystal structure of $ZnAl_2O_4$; (c) FTIR spectra; TEM images of the 5 mol% Na^+ codoped sample with a scale bar of (d) 200 nm, (e) 50 nm, and (f) 20 nm, respectively; (g) HRTEM image of the 5 mol% Na^+ codoped sample (scale bar = 5 nm); and (h) size distribution curve.

(ESI†). TEM images of the 5 mol% Na^+ codoped $ZnAl_2O_4$ sample having maximum UCL were collected, which revealed an almost spherical morphology and average particle size of 56.0 nm (Fig. 1(d)–(f)). The HRTEM image shows (111) lattice planes of $ZnAl_2O_4$ with a *d*-spacing of 0.4667 nm, consistent with the spinel structure (Fig. 1(g)), which indicates the high crystallinity of the sample. The particle size distribution curve is given in Fig. 1(h) and particle sizes are found in the range of 20 to 130 nm.

2.3. Time resolved photoluminescence

2.3.1. Visible UC measurements under 980 nm excitation. The visible UC emission spectra of a series of $ZnAl_2O_4$:1%Ho^{3+}, 5%Yb^{3+}, *x*%Na^+ (*x* = 0, 1, 2, 5, 7 and 10 mol%) samples under 980 nm laser excitation are presented in Fig. 2(a). Ho^{3+} ions exhibited characteristic emission bands in the blue, green, red, and NIR regions but the singly Ho^{3+} doped $ZnAl_2O_4$ showed very weak emissions in green and red regions due to the lack of efficient excitations that could be only observed at very high incident laser power. The emission spectra of codoped $ZnAl_2O_4$:Ho^{3+}, Yb^{3+}, Na^+ samples display strong green and red emissions at (540, 550) and 669 nm, respectively. The green emission centered at 540 and 550 nm and the red emission at 669 nm can be ascribed to $^5F_4$ and $^5S_2 \rightarrow {}^5I_8$ and $^5F_5 \rightarrow {}^5I_8$ transitions of Ho^{3+} ions, respectively.[25,29,42] However, the emissions in the blue region were not observed in the singly doped $ZnAl_2O_4$:Ho^{3+} sample.

The peak positions were not altered by Yb^{3+} codoping and the boost in UCL intensity occurred as a result of energy transfer between Yb^{3+}–Ho^{3+} pairs that can be ascribed to efficient absorption of 980 nm photons by Yb^{3+} ions. The 980 nm NIR light can efficiently excite Yb^{3+} ions in the ground

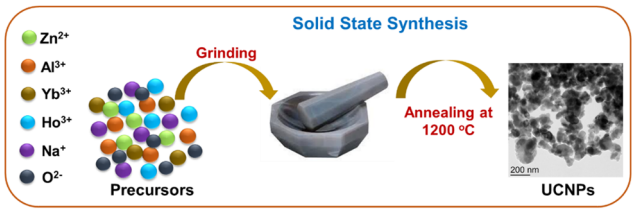

Scheme 1 Schematic illustration demonstrating the synthesis of $ZnAl_2O_4$: 1%Ho^{3+}, 5%Yb^{3+}, *x*%Na^+ (*x* = 0, 1, 2, 5, 7, and 10 mol%) UCNPs.

state $^2F_{7/2}$ to the $^2F_{5/2}$ excited state due to the large absorption cross-section of Yb^{3+} for 980 nm photons.[35,36,47] The energy released during the de-excitation of photons from the $^2F_{5/2}$ energy level of Yb^{3+} ions was transferred to Ho^{3+} ions in their ground state ($^5I_8$). The schematic energy level diagram in Fig. 3(d) represents different mechanisms of energy transfer between Yb^{3+}–Ho^{3+} pairs, which include energy transfer upconversion (ETU), ground state absorption (GSA), excited state absorption (ESA), and cooperative energy transfer (CET).[36] The $^5I_6$ excited state of Ho^{3+} ions was populated *via* the GSA mechanism due to energy transfer from Yb^{3+} ions (ETU_I). The Ho^{3+} ions in the $^5I_6$ energy level can populate the $^5F_4/^5S_2$ excited states by mechanisms, (i) the absorption of 980 nm photons by Ho^{3+} ions through ESA, and (ii) energy transfer from Yb^{3+} ions through ETU_{II}. Moreover, the ETU_{II} mechanism is usually more probable in comparison to ESA that is more feasible at higher pump powers.[35] The excited Ho^{3+} ions present in the $^5F_4/^5S_2$ energy levels relax to the ground state ($^5I_8$) by emitting photons of 540 and 550 nm (green emission), and by non-radiative relaxation (NR) to the $^5F_5$ state, followed by the emission of a 669 nm photon (red emission).

2.3.2. Effect of Na^+ doping on visible UCL and decay lifetimes. The emission intensity improved by many folds on Na^+ codoping as demonstrated in Fig. 2(a) and (b), which can be attributed to the lowering of the symmetry around Ho^{3+} ions and perturbation in the local environment by the incorporation of Na^+ ions.[33,35] The same can also be attributed to the compensation of zinc vacancies formed due to the aliovalent substitution of trivalent lanthanides at divalent zinc sites *via* monovalent sodium codoping.[34] In the Na^+ codoped $ZnAl_2O_4$ samples, the green and red peaks appeared at 550 and 669 nm, similar to the singly doped Ho^{3+} and Ho^{3+}/Yb^{3+} codoped samples. The increment in the UC emission intensity was noticed up to a codoping concentration of 5 mol% of Na^+ ions (Fig. 2(b)). A further increase in the doping concentrations of Na^+ ions was detrimental to UCL due to concentration quenching, observed for 7 and 10 mol%. With the rise in the codoping Na^+ concentrations, the Ho^{3+} ions are located at a distance shorter than the critical distance and non-radiative relaxations occur by the transfer of the excitation energy by multipolar interactions.[42,43] The contribution in observed upconversion emissions due to the presence of Ho^{3+} ions in the Yb_2O_3 impurity phase was also explored by recording the UC emission

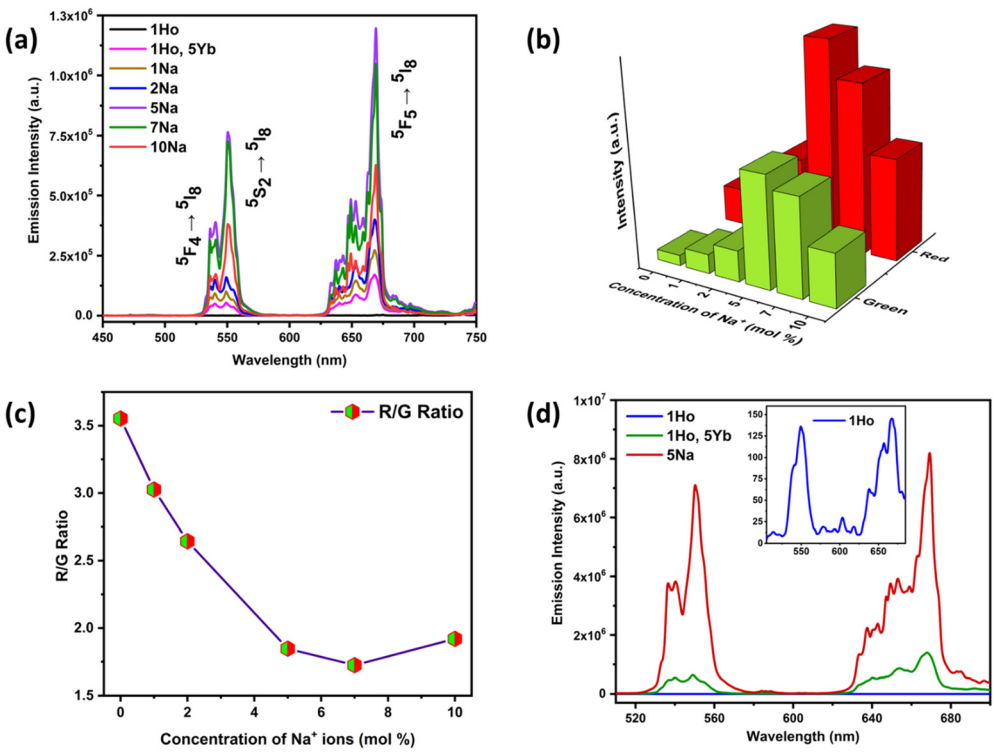

Fig. 2 (a) UC emission spectra of codoped $ZnAl_2O_4$:1%Ho^{3+}, 5%Yb^{3+}, *x*%Na^+ (*x* = 0, 1, 2, 5, 7 and 10 mol%) samples under 980 nm laser excitation at a laser power of 0.310 W, (b) the variation in green and red UC emission intensities, (c) change in R/G ratio with the change in the codoping concentration of Na^+ ions, and (d) comparison of UC emission in singly doped 1%Ho^{3+}, codoped 1%Ho^{3+}/5%Yb^{3+}, and Ho^{3+}/Yb^{3+}/5%Na^+ samples of $ZnAl_2O_4$ at a pump power of 2.82 W.

spectra of Yb_2O_3:1% Ho^{3+}, 5% Na^+ synthesized under similar synthetic conditions. We observed a very feeble emission in the codoped Yb_2O_3 sample compared to the codoped $ZnAl_2O_4$:1%Ho^{3+}, 5%Yb^{3+}, 5%Na^+ sample even at a high laser power of 2.82 W (Fig. S5, ESI†). Hence, the strong upconversion emissions can be ascribed to Ho^{3+} ions present in the major $ZnAl_2O_4$ phase.

The integral intensity ratios for red and green UC emissions were calculated for all the codoped Ho^{3+}/Yb^{3+}/Na^+ samples of $ZnAl_2O_4$, in the region of 620–695 nm for red and 520–580 nm for green UC emission. Interestingly, the red to green UC emission ratio (R/G ratio) showed a significant decrease up to a codoping concentration of 7 mol% of Na^+ ions from 3.22 to 1.72 as the Na^+ ion concentration increases and then, a slight rise in R/G ratio is observed for 10 mol% (Fig. 2(c)). This suggests that the green UC emission intensity got amplified by higher times in comparison with the red UC emission. This was very much visibly evident from Fig. S6a and S7 (ESI†) as well where the Commission Internationale de L'Eclairage (CIE) coordinate values hinge towards the yellowish-red region and become more and more greener at higher sodium ion concentration, resulting in the change of CIE coordinates from (0.438, 0.535) to (0.387, 0.604). Thus, the color tunability in the $ZnAl_2O_4$:Ho^{3+}, Yb^{3+}, Na^+ phosphor material has been achieved and the color purity values increased from 92.4% to 98.0% by variation in the codoping concentrations of Na^+ ions. Multicolor emissive UCNPs have potential for multiplexed bioimaging and multiple signals can be acquired simultaneously, which improves the bioimaging resolution. The description for color purity and correlated color temperature (CCT) calculations are provided in Section S2.5 (ESI†). Hence, the codoping of Na^+ ions is a potential strategy to tune the UC emission along with enhancing the UC emission intensity.

The UC emission spectra of the doped $ZnAl_2O_4$:1%Ho^{3+} sample demonstrated peaks at 550 and 669 nm with a very low signal to noise ratio at a pump power excitation of 0.310 W. Therefore, the spectra of doped $ZnAl_2O_4$:1%Ho^{3+} were recorded at a higher pump power of 2.82 W for showcasing the effect of Yb^{3+} and Na^+ codoping in the Ho^{3+} doped sample. The comparison of singly doped 1%Ho^{3+}, codoped 1%Ho^{3+}/5%Yb^{3+}, and Ho^{3+}/Yb^{3+}/5%Na^+ samples of $ZnAl_2O_4$ is shown in Fig. 2(d) and the inset demonstrates the zoomed in UC emission spectra of the $ZnAl_2O_4$:1%Ho^{3+} sample. In our case, the green and red emissions in the codoped $ZnAl_2O_4$:Ho^{3+}–Yb^{3+} samples were enhanced by 4×10^3 times and 6.9×10^3 times, respectively. Moreover, we have achieved a remarkable increment by 3.5×10^4 times in the green and 3.2×10^4 times in the red UC emissions *via* Na^+/Yb^{3+} codoping. The codoping of Na^+ ions in the codoped 1%Ho^{3+}/5%Yb^{3+} sample resulted in an enhancement of green and red UC emissions by 8.6 and 5.0 times, respectively. Table S2 (ESI†) tabulates some of the recent reports wherein non-fluorescent metal ions are used as crystal field modulators to enhance UC emission in Ho^{3+}–Yb^{3+} codoped phosphors. It was quite evident from this table that the current spinel-based phosphor with sodium ion as a field modulator and charge compensator not only emerged victorious in terms of intensity enhancement but also was being able to produce UV-C and visible UC and short-wave IR by down conversion as well as Na^+ concentration and laser power-dependent induced tunability. At the same time, our material showed the potential to serve as a theranostic and anticancer agent. The luminescence decay curves for 550 and 669 nm UC emissions are shown in Fig. S8 (ESI†) and the detailed analysis and consequences of Na^+ codoping on the decay lifetimes are presented in Section S2.6 (ESI†).

2.3.3. Pump power dependence of red and green UC emissions. As the NIR pump power was increased, the 550 nm (green) and 669 nm (red) UC emissions became more intense, as depicted in Fig. 3(a). Interestingly, the R/G ratio decreased with the increase in the laser power until 1.32 W and reached saturation at higher powers. This indicated that in the lower power domain the laser excitation intensity could affect the relative UCL intensity of both the green and red emission but the former increases by a larger factor than the latter (Fig. 3(b)). The R/G ratio decreased from 3.42 to 1.17 on changing the laser power from 0.062 to 1.32 W. Under 980 nm excitation at different representative laser powers, the obtained corresponding CIE chromaticity coordinates are shown in Fig. S6b (ESI†). The color coordinates at low laser power displayed more of yellowish-red light and became greener at higher laser power. The mechanism of UC emission (Fig. 3(d)) suggests the involvement of multi-photons to populate the excited states and the mechanism of UCL could be unraveled by studying the NIR laser power-dependent intensity of UC emissions. In order to find the number of photons populating the ($^5F_4$, $^5S_2$) level for green and $^5F_5$ level for red UC emissions, the emission spectra were recorded at different laser powers. The UC emission intensity (I) for a UC process is correlated with the incident pump power (P) as

$$I \propto P^n \quad (1)$$

where n represents the number of photons involved in UC emission. As depicted in Fig. 3(c), the slope value is 1.81 for green [($^5F_4$, $^5S_2$) → ($^5I_8$)] and 1.32 for red ($^5F_5$ → $^5I_8$) emissions in a lower laser pump power range of 0.062–0.310 W. This suggests the involvement of two photons in the stimulation of Ho^{3+} ions into their ($^5F_4$, $^5S_2$) and $^5F_5$ excited states. It is noteworthy that on increasing the pump power, the slope value (n) for green UC emission decreases to 1.10 in the range of 0.310–0.972 W, and reaches 0.69 on further increase in the laser power in the range of 0.972–2.82 W. Similar observations were noted for the red UC emissions; the slope value decreases to 0.89 in the range of 0.310–0.972 W, and attains a value of 0.65 at higher pump power. The decrease in slope value with increasing the pump power can be ascribed to the saturation effects prominent at higher pump powers.[29,42,43]

2.3.4. UV-C and blue UC emissions under 980 nm excitation. The upconversion of NIR radiation into UV-C photons offers several advantages in drug delivery in deeper tissues, photodynamic therapy (PDT), optical energy storage, and catalysis.[48] Fig. 4(a) reveals the short wavelength UV and blue UC emission spectra of $ZnAl_2O_4$:1%Ho^{3+}, 5%Yb^{3+},

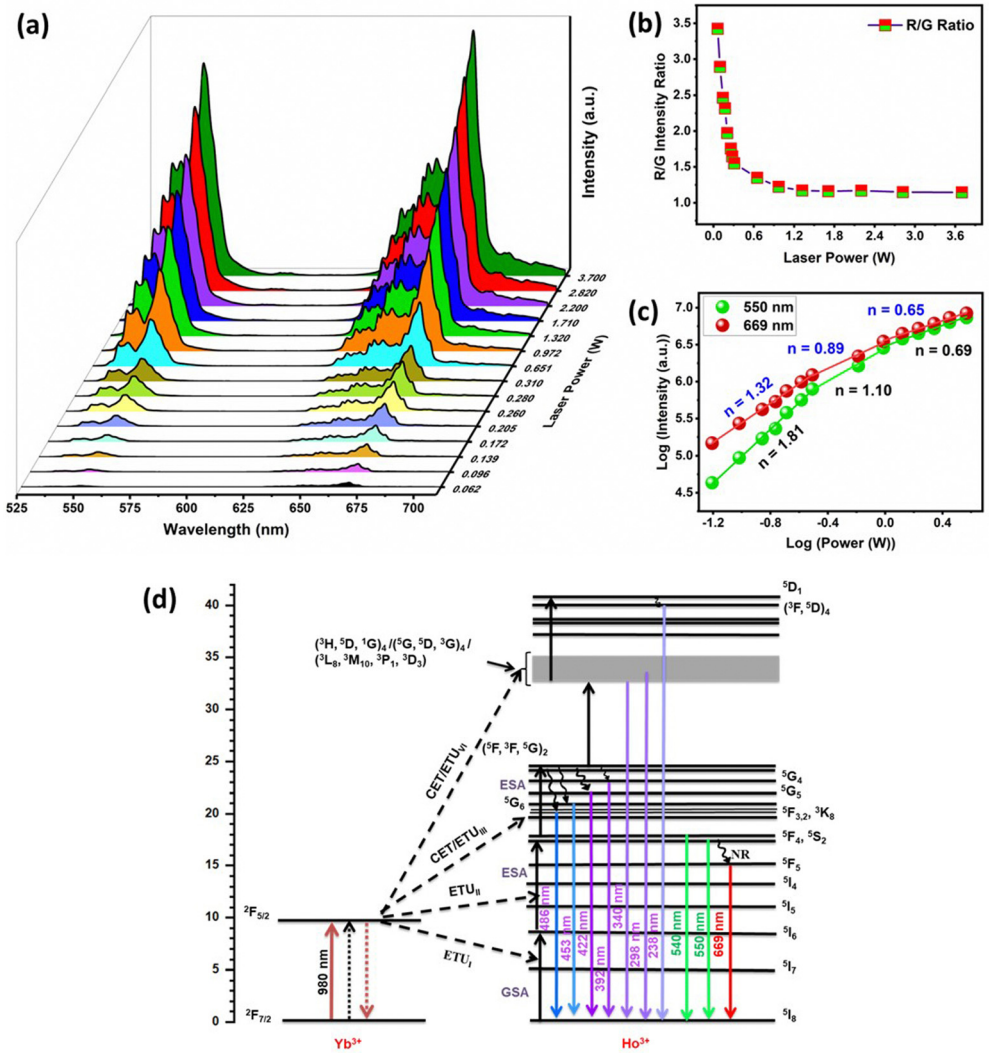

Fig. 3 (a) UC emission laser power dependence of $ZnAl_2O_4$:1%Ho^{3+}, 5%Yb^{3+}, 5%Na^+, (b) the R/G ratio variation with increasing excitation laser powers, (c) the dual logarithmic plots between the UC emission integral intensity (550 and 669 nm) and excitation power (W), and (d) schematic energy level diagrams of Ho^{3+} and Yb^{3+} ions and the mechanisms involved in visible, blue, and UV-C UC emissions on excitation at 980 nm.

x%Na^+ (x = 0, 1, 2, 5, 7 and 10 mol%). UV UC emissions were not displayed by the $ZnAl_2O_4$:1% Ho^{3+} sample under the 980 nm laser excitation with a pump power of 2.20 W due to inefficient excitations. It is noteworthy that with the doping of Yb^{3+} as a sensitizer, an intense UC band appeared at 238 nm, which lies perfectly in the germicidal range.[28,49] The intense UC band peaked at 238 nm along with other weak bands at 298, 392, and 422 nm can be ascribed to the (^{3}F, ^{5}D)$_4$ → ^{5}I$_8$, (^{3}L$_8$, ^{3}M$_{10}$, ^{3}P$_1$, ^{3}D$_3$) → ^{5}I$_8$, (^{5}F, ^{3}F, ^{5}G$_2$) → ^{5}I$_8$, ^{5}G$_4$ → ^{5}I$_8$, and ^{5}G$_5$ → ^{5}I$_8$, respectively (Fig. 4(b)). Such an intense short wavelength UV-C UC emission for Ho^{3+} ion doped phosphors has not been discovered so far to the best of our knowledge. As shown in Fig. 3(d), the mechanism of the observed UV UC emission is attributed to ETU_{III}/CET from Yb^{3+} ions, resulting in the excitation of the Ho^{3+} ions to the (^{5}F, ^{3}F, ^{5}G)$_2$ states followed by non-radiative decay processes and emission of 486, 453, 422, and 392 nm photons on radiative relaxation.[29,50,51] In fact, the UC emissions had low signal to noise ratio and UCL is enhanced at higher laser powers; the emission spectra showing UC bands at 486 and 453 nm are presented in Fig. S9 (ESI†). The ETU_{IV} process excites the Ho^{3+} ions to the (^{3}H, ^{5}D, ^{1}G)$_4$, (^{5}G, ^{5}D, ^{3}G)$_4$, (^{3}L$_8$, ^{3}M$_{10}$, ^{3}P$_1$, ^{3}D$_3$) state denoted by a grey band in Fig. 3(d), as all these states are thermally coupled due to close energies.[29] The excited Ho^{3+} ions from these states radiatively relax to the ground state, and the resultant UV UC band at 298 nm is comprised of transitions from the (^{3}L$_8$, ^{3}M$_{10}$, ^{3}P$_1$, ^{3}D$_3$) states to the ^{5}I$_8$ state.[29,52] The intense UV-C band at 238 nm could be attained when the ^{5}D$_1$ state is populated *via* ETU_{IV}/CET between the Yb^{3+}–Ho^{3+} pairs, and Ho^{3+} ions relax *via* non-radiative decay to the (^{3}F, ^{5}D)$_4$ state, followed by radiative relaxation to the ground state (^{5}I$_8$) by emitting 238 nm photons.[29,50,51]

2.3.5 Effect of Na^+ ion on UV-C and blue UC emissions. The codoping of Na^+ resulted in a significant enhancement in the UV-C UC emission intensity and emerged as a potential strategy for improving the UCL of UV UC materials to obtain phosphors

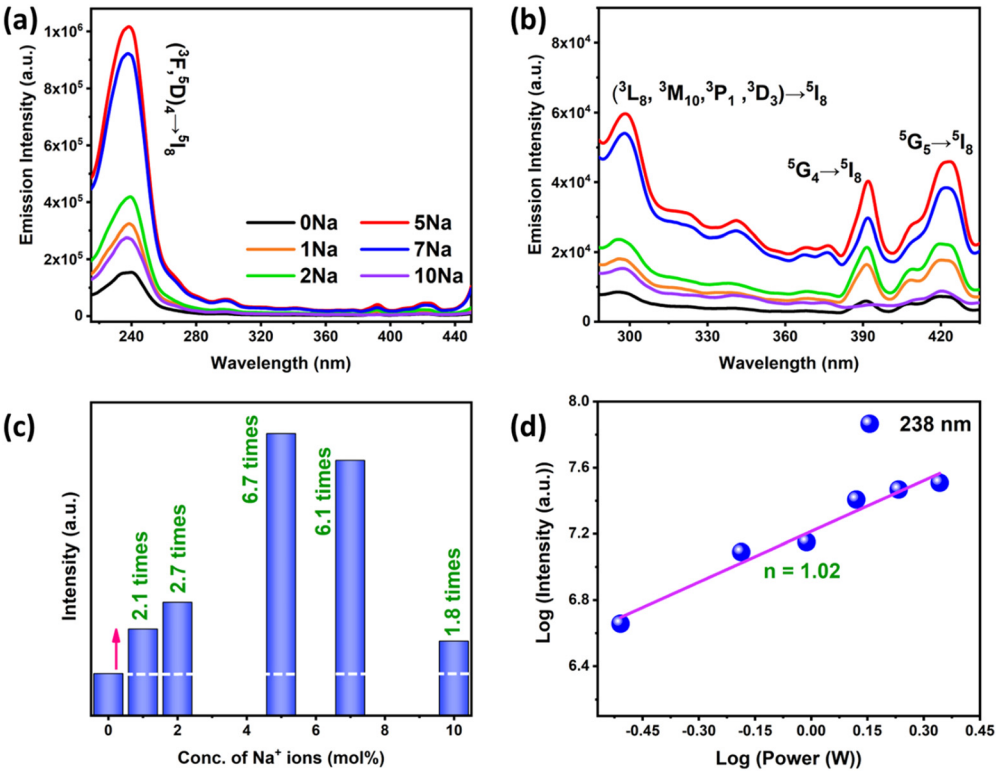

Fig. 4 (a) UV and blue UC emission spectra of codoped $ZnAl_2O_4$:1%Ho^{3+}, 5%Yb^{3+}, *x*%Na^+ (*x* = 0, 1, 2, 5, 7, and 10 mol%) samples under 980 nm laser excitation at a power of 2.20 W, (b) zoomed in UV and blue emissions in 290–430 nm region, (c) variation in UV-C emission with changing Na^+ concentration, and (d) the dual logarithmic plots between the UV-C UC emission intensity (238 nm) and laser excitation power (W).

with desired UCL properties. The reports on UC materials exhibiting such UV-C emissions are very few in the literature and most of them focussed on Pr^{3+} doped materials. Thus, this study reveals the ability of $ZnAl_2O_4$:Ho^{3+}/Yb^{3+}/Na^+ codoped phosphors to emit in the UV-C region, which makes them a potential candidate for applications, such as the bacterial decontamination of water, virus deactivation, photo medicine.[28] As depicted by Fig. 4(a) and (c) the UV and blue UC bands become significantly more intense with increasing Na^+ ion concentration up to an optimal concentration of 5 mol%. Then, a dip in the emission intensity was noticed for 7 and 10 mol% Na^+ concentration and the same was a consequence of concentration quenching as the relative distance between Ho^{3+} ions decreased, leading to a decrease in radiative processes.[42] The integral intensity of 238 nm radiation in the codoped 1%Ho^{3+}/5%Yb^{3+}/5%Na^+ sample was enhanced by 6.7 times compared to the UC intensity attained in the codoped $ZnAl_2O_4$:1%Ho^{3+}/5%Yb^{3+} sample without Na^+ ions. The boost in the UV-C UC emission on codoping Na^+ ions can be ascribed to a decrease in the defects that act as quenching centers by charge compensation along with their ability to act as crystal field modulators and making f → f transition more allowed. The decay curves for the UV-C UC emission at 238 nm are depicted in Fig. S10 (ESI†) and the observations are described in Section S2.6 (ESI†).

2.3.6. Pump power dependence of UV-C UC emission at 238 nm. The UC emission spectra monitored in the 215–450 nm range were recorded under 980 nm excitations with different laser powers (W) and a monotonic increase was observed in UV-C UC intensity with laser power. The integral intensities were evaluated for the different laser powers for the codoped 1%Ho^{3+}/5%Yb^{3+}/5%Na^+ sample (the one with maximum UCL output) of $ZnAl_2O_4$, in the region of 215–265 nm for 238 nm UV-C UC emission. The logarithmic plot between the UV-C UC emission intensities and different laser powers was plotted and the slope value (Fig. 4(d)) obtained for 238 nm UV-C radiation, 1.02, was in the full power range (0.310–2.20 W), which was lower than the number of photons participating in the mechanism of populating the excited states and $(^3F, {}^5D)_4 \rightarrow {}^5I_8$ transition (Fig. 3(d)). The lower slope value implies the presence of supersaturation effects occurring due to faster UC rates compared to the radiative decay rates.[53]

2.3.7. Role of Na^+ ion in UCL of Ho^{3+}: positron annihilation lifetime spectroscopy. The improvement in the UC emission intensity for both the visible and UV UC achieved by codoping of Na^+ can be attributed to two major processes, crystal field modulation and charge compensation.[32,34,35,37,54] The Na^+ ions locating nearby Ho^{3+} ions lowered down the symmetry around Ho^{3+} ions, and thus intraconfigurational f–f transitions became partially allowed and thus, an increase in emission intensity was attained. In addition, the doping of Na^+ was responsible for charge compensation as Na^+ ions were incorporated in the defect sites. The crystal defects were inevitable during the synthesis process and the substitution

of Zn^{2+} ions by Ho^{3+} and Yb^{3+} ions further increases the defects (zinc vacancies). The generation of more defects becomes detrimental to UCL as defects act as the quenching centers, leading to an increment in non-radiative relaxations of excited Ho^{3+} ions to the ground state ($^5I_8$) by transfer of energy to energy reducing defect sites *via* multipolar interaction.[55]

The occupation of Zn^{2+} sites by Ho^{3+} and Yb^{3+} ions creates Zn^{2+} deficiencies in the $ZnAl_2O_4$ matrix and charge imbalance. The codoping with Na^+ ions maintains the charge balance:

$$4Zn^{2+} = Ho^{3+} + Yb^{3+} + 2Na^+ \quad (2)$$

Consequently, the Na^+ doping lowers the structural defects, thereby reducing the probability of non-radiative processes. Hence, the UCL increases by increasing the doping concentration of Na^+ ions until 5 mol%. The decrease in UCL at higher Na^+ ion concentration was observed and at higher doping concentrations Na^+ ions were compelled to occupy interstitial sites, resulting in the generation of new defect centers that reduces UCL.[55] To prove it further and get a better insight, we carried out PALS measurement, which is considered one of the most sensitive techniques for understanding defect evolution in inorganic materials. The analysis of PALS data is provided in detail in Section S2.7 (ESI†). The first two lifetime components and their intensities in all the samples are given in Fig. S11 (ESI†) as a function of $\%Na^+$ codoping in $ZnAl_2O_4$ doped with 1%Ho and 5%Yb. PALS results suggest that initial codoping of Na^+ partially removes defects, while at concentration higher than 5%, the charge compensation is not effective. The size of Na^+ is higher than that of all the other ions and it seems to be causing distortions in the lattice that is reflected as an increase in average positron lifetime. The positron lifetimes decreased with codoping of Na^+ initially and increased later. The average positron lifetime too increased more drastically at higher concentration of Na^+. The positron lifetimes seem to be inversely correlated with PL that lower the positron lifetimes, higher the emission or the defects or cation vacancy removal is enhancing the PL intensities.

The Kroger–Vink notation for either Ho^{3+} or Yb^{3+} substituted at Zn^{2+} should be represented with eqn (3) and (4) as mentioned below:

$$2Ho^{\bullet\bullet\bullet} + 3Zn^{\bullet\bullet}_{Zn} \leftrightarrow 2Ho^{\bullet}_{Zn} + V''_{Zn} \quad (3)$$

$$2Yb^{\bullet\bullet\bullet} + 3Zn^{\bullet\bullet}_{Zn} \leftrightarrow 2Ho^{\bullet}_{Zn} + V''_{Zn} \quad (4)$$

It is reported that these negatively charged zinc vacancies provide additional pathways for non-radiative transitions and successfully quench the UC and DC luminescence by absorbing the photon energy emitted by the active holmium ion centres.[56] The inclusion of sodium ions increased the UCL emission intensity as they decreased the amount of negatively charged zinc vacancies by acting as a charge compensator created as a result of aliovalent substitution of Ho^{3+}/Yb^{3+} at the Zn^{2+} site as well as by acting as a crystal field modulator. But it was the significant reduction in the density of cation vacancies that is considered the main reason for the enhancement in UCL/DCL intensity on sodium ion codoping. In addition, the effect of Ho^{3+}, Yb^{3+}, and Na^+ ion codoping in the zinc aluminate lattice has been investigated using DFT calculations and the results are discussed in Section S2.8 (ESI†) and we have analysed the electronic structure (Fig. S12a–c, ESI†).

2.3.8. NIR DC Emission under 980 nm excitation. The DC emission spectra of doped Ho^{3+} and codoped $ZnAl_2O_4$:1%Ho^{3+}, 5%Yb^{3+}, x%Na^+ (x = 0, 1, 2, 5, 7, and 10 mol%) samples scanned in the range of 1470–1620 nm were recorded under 980 nm excitation and are shown in Fig. S13a (ESI†). The NIR DC

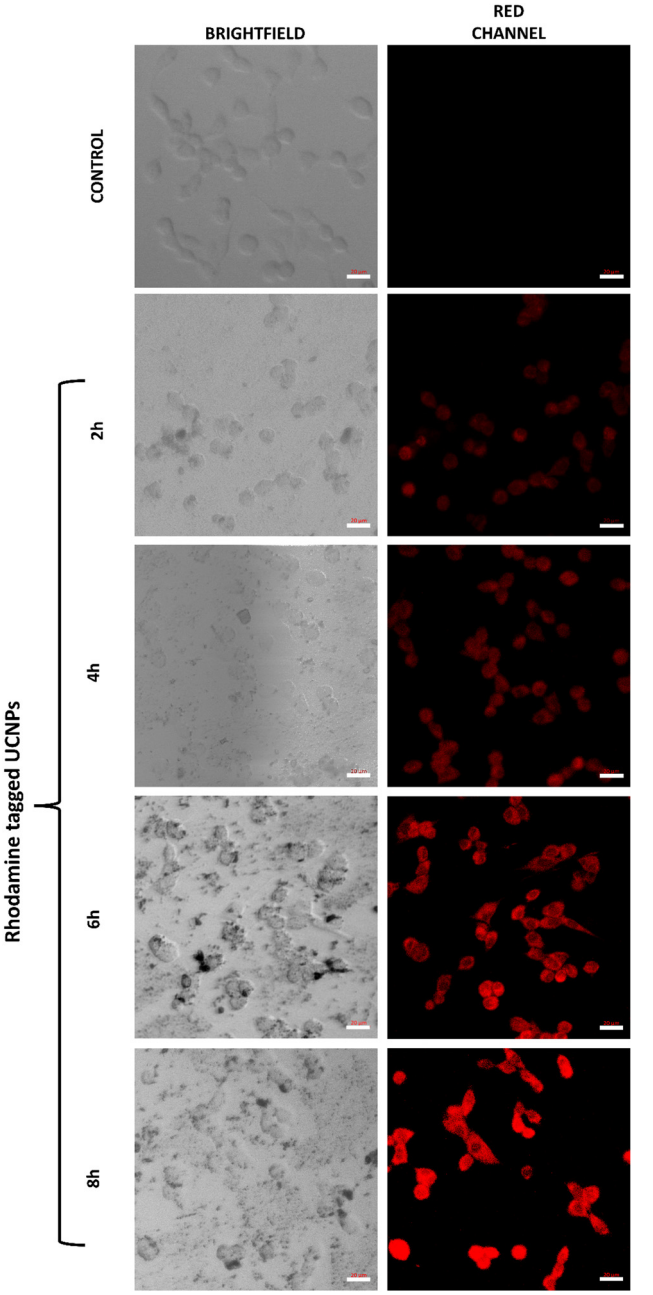

Fig. 5 Cellular uptake of $ZnAl_2O_4$:1%Ho^{3+}, 5%Yb^{3+}, 5%Na^+ UCNPs as determined in C6 glioma cells after different time periods using confocal microscopy. Scale: 20 μm.

emissions were not observed in the singly doped $ZnAl_2O_4$:1%Ho^{3+} sample due to the inefficient absorption of 980 nm photons. The DC emission intensity of the broad band in the NIR-II window peaked at 1600 nm, and increased on codoping of 1 mol% of Na^+ ions, and further addition of Na^+ ions proved to be detrimental to NIR DC emissions (Fig. S13b, ESI†). The band can be attributed to $^5I_5 \rightarrow {}^5I_7$ transitions observed when excited Ho^{3+} ions in $^5F_4$ and $^5S_2$ states populate the intermediate $^5I_5$ state *via* the non-radiative relaxation mechanism. The NIR bands due to other transitions from intermediate levels were not observed on 980 nm excitation. The NIR-II spectral window is gaining more attention of the researchers due to its potential in disease screening and bio-imaging by taking advantage of deep tissue penetration and high resolution.[57]

2.4. The photothermal effect of $ZnAl_2O_4$:1%Ho^{3+}, 5%Yb^{3+}, 5%Na^+ UCNPs

As a consequence of the high NIR absorbing property, we anticipated that $ZnAl_2O_4$:1%Ho^{3+}, 5%Yb^{3+}, 5%Na^+ UCNPs would demonstrate remarkable photothermal behaviour to act as a photothermal agent for destructing the cancer cells. To evaluate their photothermal effect, 1 mg mL^{-1} solution of UCNPs was exposed to a 980 nm laser for 10 mins and any increment in the surrounding media temperature was recorded using a thermometer. It was interesting to observe that the temperature of UCNP solution increased from 20 °C to 50 °C in a time span of 10 min (Fig. S14, ESI†), confirming the photothermal nature of the UCNPs, as compared to the control water sample, where no significant temperature enhancement was observed.[58] The results were indicative of the conversion of light energy into thermal energy on laser irradiation of the UCNPs subsequently leading to the generation of heat that could aid in the photothermal triggered death of the cells in tumor tissues. Thus, this upconvertible nanophosphor has the potency to serve as a photothermal based therapeutic modality in cancer.[59]

2.5. Cellular uptake studies of the UCNPs performed in C6 cells

To determine the ability of our UCNPs to get internalized into the cancer cells, their cellular uptake behaviour was evaluated in C6 glioma cells. For the study, cells were treated with rhodamine tagged UCNPs at a concentration of 40 μg mL^{-1} and uptake was analysed *via* confocal microscopy. As indicative of our results (Fig. 5), a time-dependent uptake of UCNPs was observed in the cells. The red fluorescence due to rhodamine depicted a successful distribution of our UCNPs in the C6 cells. As compared to the control cells, a higher fluorescence signal was observed in the cells exposed to the UCNPs as the time lapsed from 2 h to 8 h.[60,61]

2.6. Biocompatibility study of the UCNPs performed in fibroblast cells

For cellular experiments, UCNPs were properly dispersed in aqueous media following sonication. We further carried out dynamic light scattering based studies (Fig. S15, ESI†) whose results depicted a fair dispersion of the particles in aqueous media with a PDI of 0.4. For a system to be translated as a therapeutic modality or as a drug delivery carrier in biological tissues, it is highly essential that the system depict promising compatibility with a healthy biological environment. Thus, the cytotoxicity of the UCNPs was determined in non-cancerous fibroblast L929 cells. As shown in Fig. 6(a), the percent cell viability of L929 fibroblast cells incubated for 24 h with the varying concentration of UCNPs was observed to be equal to or greater than 100%. Thereby, the results indicated an excellent bio and cytocompatibility of the as prepared UCNPs in L929 cells.[62]

2.7. Anti-cancer efficacy of the UCNPs determined in C6 glioma cells

After the confirmation of a superior cellular uptake and favourable *in vitro* biocompatibility, UCNPs were next evaluated for their anticancer efficacy in C6 glioma cells by MTT assay. The

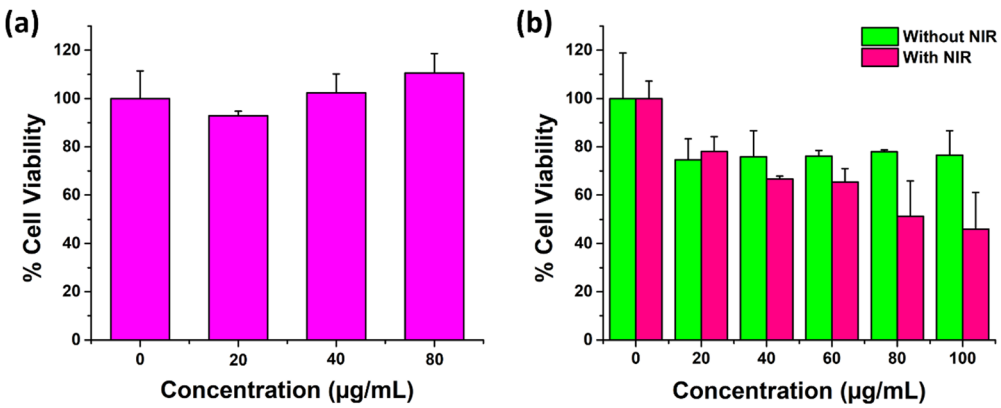

Fig. 6 (a) Biocompatibility of $ZnAl_2O_4$:1%Ho^{3+}, 5%Yb^{3+}, 5%Na^+ UCNPs as determined in L929 fibroblast cells by MTT assay for a period of 24 h; (b) anticancer efficacy of $ZnAl_2O_4$:1%Ho^{3+}, 5%Yb^{3+}, 5%Na^+ UCNPs determined in C6 glioma cells for 24 h. The results present a higher cancer cell killing ability of the particles in the presence of the NIR laser. Graphs represent mean ± SD (n = 3).

study was conducted at different concentrations of UCNPs in two groups, *viz.*, without NIR and with NIR (980 nm NIR, at 1 W cm^{-2} for 5 mins) laser exposure in C6 glioma cells for 24 h. The results indicated that the percent cell viability of C6 cells exposed to 100 μg mL^{-1} UCNPs decreased to approximately 46% under NIR laser exposure as compared to the 76.5% observed in the absence of the NIR laser. Also, the cell viability decreased concomitantly with an increase in the particle concentration from 20 μg mL^{-1} to 100 μg mL^{-1} in a gradual fashion (Fig. 6(b)). From these results, it was observed

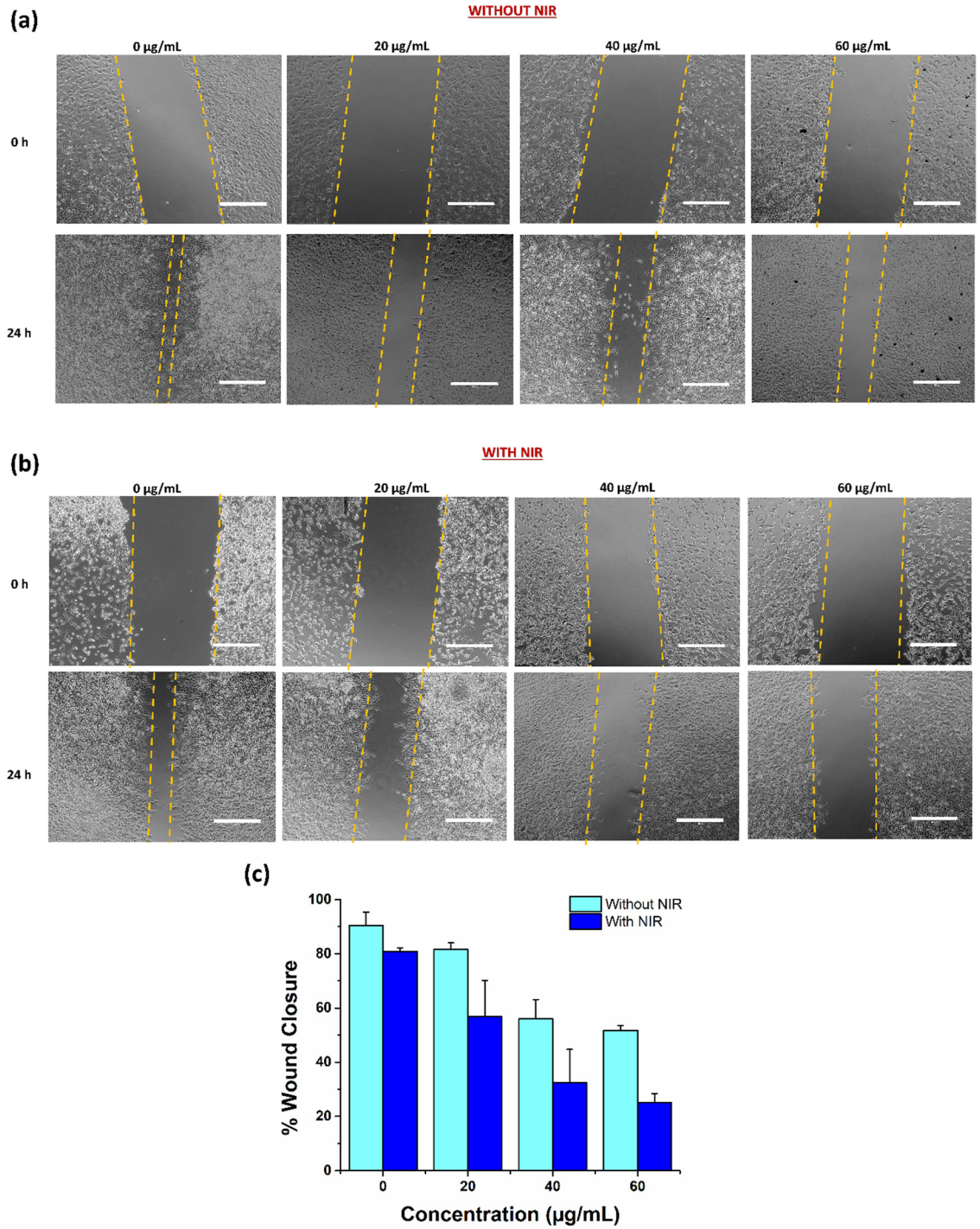

Fig. 7 (a) Scratch wound healing assay images of C6 glioma cells treated with varying concentration of $ZnAl_2O_4$:1%Ho^{3+}, 5%Yb^{3+}, 5%Na^{+} UCNPs without an NIR laser (980 nm, 1 W cm^{-2} for 5 min); (b) scratch wound healing assay images of C6 glioma cells treated with varying concentration of $ZnAl_2O_4$:1%Ho^{3+}, 5%Yb^{3+}, 5%Na^{+} UCNPs exposed to an NIR laser (980 nm, 1 W cm^{-2} for 5 min); (c) cell migration rates were estimated as percentage of wound closure calculated with reference to the control cells after 24 h time. Scale: 400 μm. Graphs represent mean ± SD (n = 3).

that the $ZnAl_2O_4$:1%Ho^{3+}, 5%Yb^{3+}, 5%Na^+ UCNPs depicted a concentration dependent cellular toxicity in the C6 cell line, which was further enhanced upon NIR irradiation due to the activation of their photothermal properties. As indicative of the photothermal property of our UCNPs, the heat generated through laser irradiation was the underlying cause for a higher observed cancer cell killing ability of the particles in the presence of the laser.[60,63]

2.8. Scratch wound healing assay

After the successful depiction of anticancer ability of UCNPs under NIR conditions, we next investigated their anti-migratory potential in C6 glioma cells by a scratch wound healing assay. Scratch assay has been reported to be a standard method to study cell migration. The ability of the cells to migrate across the wound in the presence of treatment at different concentrations with NIR and without NIR was studied to explore the anti-metastatic activity of our UCNPs.[64] The results as demonstrated in Fig. 7(a) and (b), indicated a fortunate concentration dependent inhibition of cancer cell migration under NIR exposure in C6 cells. After 24 h of incubation, the wound distance was measured and analysed using the ImageJ software. Higher inhibition in C6 cell migration was observed with a higher concentration of treatment in the presence of a 980 nm laser. The wound healing capability of cells at 60 μg mL^{-1} after 24 h of incubation was uncertain and insignificant, resulting in a diminished migration potential of cells as compared to the control cells. Further, quantitatively, percentage wound healing was estimated using the ImageJ software, which depicted an insignificant wound closure with only 25.17% of closure in cells treated with 60 μg mL^{-1} UCNPs in the presence of a laser as compared to around 80% wound closure in control cells (0 μg mL^{-1}) under similar NIR conditions (Fig. 7(c)). The cell migration inhibition potential improved with increasing concentration of the UCNPs, inferring a concentration dependent anti-migratory effect, which may further strengthen their anticancer effect in glioma.[65]

2.9. Preclinical studies with intrinsically radiolabeled $ZnAl_2O_4$:1%Ho^{3+}, 5%Yb^{3+}, 5%Na^+

The radionuclidic purity of the synthesized intrinsically radiolabeled $ZnAl_2O_4$:5%Yb^{3+}, $^{166}Ho^{3+}$, 5%Na^+ (^{166}Ho is a radioactive isotope) was determined using γ-spectrometry. Only characteristic peaks corresponding to ^{166}Ho could be determined in the γ-ray spectrum (Fig. 8(a)), demonstrating its high radionuclidic purity (>99.99%) for preclinical studies. The radiochemical purity of $ZnAl_2O_4$:5%Yb^{3+}, $^{166}Ho^{3+}$, 5%Na^+ was determined using size exclusion chromatography (Fig. 8(b)). As expected, $ZnAl_2O_4$:5%Yb^{3+}, $^{166}Ho^{3+}$, 5%Na^+ was eluted in 2.5–5 mL fractions, while free $^{166}Ho^{3+}$ was eluted after 6 mL fractions. From this study, the radiochemical purity of $ZnAl_2O_4$:5%Yb^{3+}, $^{166}Ho^{3+}$, 5%Na^+ was determined to be 98.5 ± 0.7%. This was further corroborated by radio-TLC study (Fig. S16, ESI†). *In vitro* stability of intrinsically radiolabeled $ZnAl_2O_4$:5%Yb^{3+}, $^{166}Ho^{3+}$, 5%Na^+ was determined under physiological conditions over a period of ~6 half-lives of ^{166}Ho (Fig. 8(c)). During this period, the radiochemical stability decreased marginally in both the media from ~99% to 97%. This study amply demonstrated that intrinsically radiolabeled $ZnAl_2O_4$:5%Yb^{3+}, $^{166}Ho^{3+}$, 5%Na^+

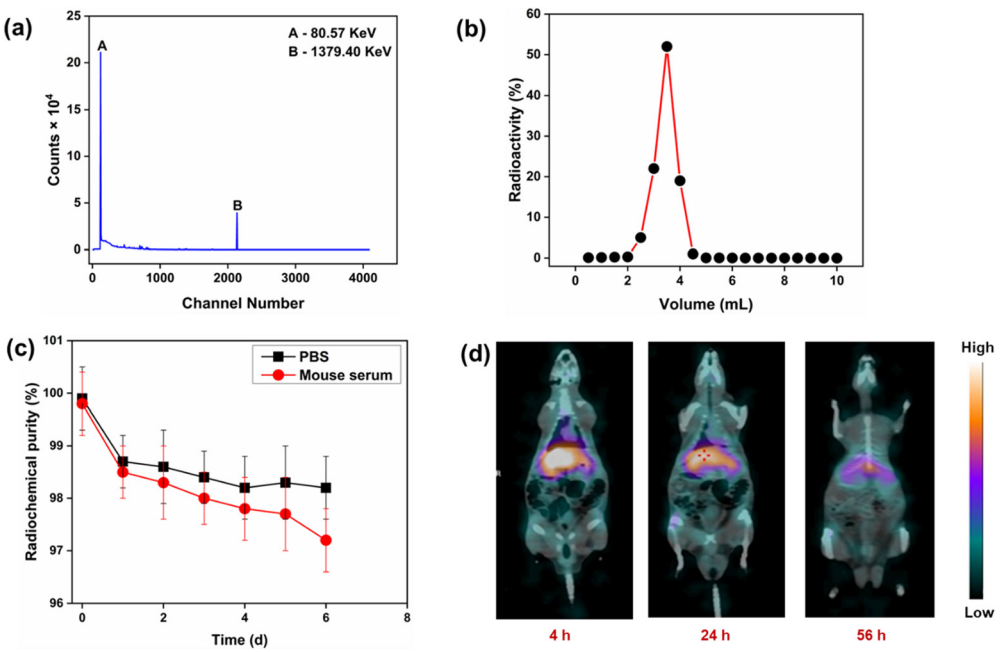

Fig. 8 (a) γ-ray spectrum of $ZnAl_2O_4$:5%Yb^{3+}, $^{166}Ho^{3+}$, 5%Na^+ showed only characteristic peaks corresponding to ^{166}Ho, (b) size exclusion chromatography pattern, (c) *in vitro* stability of intrinsically radiolabeled $ZnAl_2O_4$:5%Yb^{3+}, $^{166}Ho^{3+}$, 5Na^+ as a function of time under physiological conditions, and (d) *in vivo* SPECT/CT imaging in Wistar rats after intravenous administration of the intrinsically radiolabeled $ZnAl_2O_4$:5%Yb^{3+}, $^{166}Ho^{3+}$, 5%Na^+ formulation.

would retain its radiochemical integrity when administered for *in vivo* use.

As a proof of concept, intrinsically radiolabeled $ZnAl_2O_4$: 5%Yb^{3+}, $^{166}Ho^{3+}$, 5%Na^+ was administered intravenously in healthy Wistar rats. *In vivo* SPECT/CT imaging at different time points demonstrated the uptake of radioactivity in the liver (Fig. 8(d)). There was no uptake of radioactivity in the bladder, which indicated that the radiolabeled agent did not disintegrate *in vivo*.[66] With the passage of time, the radiolabeled $ZnAl_2O_4$:5%Yb^{3+}, $^{166}Ho^{3+}$, 5%Na^+ cleared from the biological system *via* the hepatobiliary route, which is expected for inorganic formulations.[66] This is the expected clearance pattern of radiolabeled nanoparticles when administered *in vivo*.[44,66] No accumulation of radioactivity in the skeleton or bladder was observed, which proved that the radiolabeled material maintained its integrity *in vivo* and the free $^{166}Ho^{3+}$ ions did not leach out of the radiolabeled material.[44,66] This study amply demonstrated the suitability of the radiolabeled material for use as a SPECT imaging probe. Owing to its luminescent properties, intrinsically radiolabeled $ZnAl_2O_4$: 5%Yb^{3+}, $^{166}Ho^{3+}$, 5%Na^+ could potentially be used for dual modality SPECT/optical imaging. Since ^{166}Ho is an excellent therapeutic radioisotope,[44,45] this class of intrinsically radiolabeled nanoformulations holds promise for use in theranostic applications.

3. Conclusion

The $ZnAl_2O_4$:Ho^{3+}, Yb^{3+}, Na^+ samples, upon 980 nm excitation, show intense visible and short wavelength UV-C UC emissions along with long wave infrared radiation downconversion, which have been demonstrated rarely to date in Ho^{3+}/Yb^{3+} doped UC phosphors. The Na^+ ion codoping resulted in a large boost in UCL, which is essential for practical implementations. We experimentally observed the lowering of zinc vacancies in $ZnAl_2O_4$:Ho^{3+}, Yb^{3+} on co-doping with Na^+, indicating its effective role as a charge compensator and crystal field modulator. The excellent photophysical properties, high color purity and color tunability are attainable by adjusting the composition of Na^+ ions and the incident laser power. We demonstrated the use of the intrinsically radiolabeled $ZnAl_2O_4$:$^{166}Ho^{3+}$, Yb^{3+}, Na^+ phosphor for dual-modality SPECT/optical imaging and cancer treatment.

Additionally, promising *in vitro* results were obtained with fibroblast and C6 glioma cell lines, conclusively demonstrating the biocompatibility and effective laser-triggered anticancer potential of carrier/drug-free $ZnAl_2O_4$:Ho^{3+}, Yb^{3+}, Na^+ UCNPs. The proof of concept $ZnAl_2O_4$:$^{166}Ho^{3+}$, Yb^{3+}, Na^+ SPECT imaging experiments revealed high radiochemical purity and integrity, good *in vitro* and *in vivo* stability, clearance *via* the hepatobiliary route, fast pharmacokinetics, and no detectable radioactivity accumulating in the bladder, skeleton or other organs, all of which are valuable for future work pairing ^{166}Ho with therapeutic isotopes. Further, the impressive, intense UV-C emission could be crucial in safe disinfection and medical applications, especially in a threatening crisis like the COVID-19 pandemic.

Conflicts of interest

There are no conflicts to declare.

Acknowledgements

AB and SKG would like to acknowledge Dr J. Bahadur, SSPD for providing SEM images, Dr Kathi Sudarshan for PALS measurement, Dr B. Modak for DFT calculations, Dr Manoj Mohapatra in active holmium sample preparation and Dr Arnab Sarkar, FCD for LIBS measurements. The authors acknowledge the lead role of Dr Sudipta Chakraborty, Head, Radiochemicals Section, Radiopharmaceuticals Division, Bhabha Atomic Research Centre in production of radioisotopes in the Dhruva reactor. We would like to acknowledge Dr Praveen Kumar, School of Materials Sciences, Indian Association for the Cultivation of Science, Kolkata for help in TEM measurements. JJP would like to acknowledge Har-Gobind Khorana Young Innovative Biotechnologist Award from DBT (BT/13/IYBA/2020/08) and partial support from the DBT grant BT/PR36632/NNT/28/1694/2020 and SERB-Power grant (SPG/2021/002910-G) for funding. Bhabha Atomic Research Centre (BARC) is a government of India funded research insitute and this work was funded by BARC.

References

1 J. Ferlay, M. Ervik, F. Lam, M. Colombet, L. Mery, M. Piñeros, A. Znaor, I. Soerjomataram and F. Bray, *Cancer*, 2018, **3**, 2019.
2 W. He, M. You, Z. Li, L. Cao, F. Xu, F. Li and A. Li, *Sens. Actuators, B*, 2021, **334**, 129673.
3 Y. Wang, S. Song, S. Zhang and H. Zhang, *Nano Today*, 2019, **25**, 38–67.
4 K. Zhang, Q. Zhao, S. Qin, Y. Fu, R. Liu, J. Zhi and C. Shan, *J. Colloid Interface Sci.*, 2019, **537**, 316–324.
5 C. Deng, M. Zheng, J. Xin and F. An, *J. Colloid Interface Sci.*, 2023, **651**, 384–393.
6 K. Heinzmann, L. M. Carter, J. S. Lewis and E. O. Aboagye, *Nat. Biomed. Eng.*, 2017, **1**, 697–713.
7 G. Lee and Y. I. Park, *Nanomaterials*, 2018, **8**, 511.
8 D. M. Samhadaneh, G. A. Mandl, Z. Han, M. Mahjoob, S. C. Weber, M. Tuznik, D. A. Rudko, J. A. Capobianco and U. Stochaj, *ACS Appl. Bio Mater.*, 2020, **3**, 4358–4369.
9 K. Zhang, Z. Wan, H. Jiang, X. Xiao, Q. Feng, Y. Meng and Y. Yu, *Mater. Des.*, 2021, **203**, 109597.
10 C. Wang, H. Tao, L. Cheng and Z. Liu, *Biomaterials*, 2011, **32**, 6145–6154.
11 K. Du, J. Feng, X. Gao and H. Zhang, *Light: Sci. Appl.*, 2022, **11**, 222.
12 K. Kaur, B. K. Sahu, K. Swami, M. Chandel, A. Gupta, L.-H. Zhu, J. P. Youngblood, S. Kanagarajan and V. Shanmugam, *ACS Appl. Mater. Interfaces*, 2022, **14**, 27507–27514.

13 P. Li, Y. Yan, B. Chen, P. Zhang, S. Wang, J. Zhou, H. Fan, Y. Wang and X. Huang, *Biomater. Sci.*, 2018, **6**, 877–884.
14 Y.-C. Tsai, P. Vijayaraghavan, W.-H. Chiang, H.-H. Chen, T.-I. Liu, M.-Y. Shen, A. Omoto, M. Kamimura, K. Soga and H.-C. Chiu, *Theranostics*, 2018, **8**, 1435.
15 Z. Chu, T. Tian, Z. Tao, J. Yang, B. Chen, H. Chen, W. Wang, P. Yin, X. Xia and H. Wang, *Bioact. Mater.*, 2022, **17**, 71–80.
16 J. Hu, R. Wang, R. Fan, Z. Huang, Y. Liu, G. Guo and H. Fu, *J. Lumin.*, 2020, **217**, 116812.
17 L. Zhang, C. Cao, N. Kaushik, R. Y. Lai, J. Liao, G. Wang, N. Ariotti, D. Jin and M. H. Stenzel, *Biomacromolecules*, 2022, **23**, 2572–2585.
18 N. Li, X. Wen, J. Liu, B. Wang, Q. Zhan and S. He, *Opt. Mater. Express*, 2016, **6**, 1161–1171.
19 L. Cheng, K. Yang, Y. Li, X. Zeng, M. Shao, S.-T. Lee and Z. Liu, *Biomaterials*, 2012, **33**, 2215–2222.
20 B. Dong, S. Xu, J. Sun, S. Bi, D. Li, X. Bai, Y. Wang, L. Wang and H. Song, *J. Mater. Chem.*, 2011, **21**, 6193–6200.
21 S. Wen, J. Zhou, K. Zheng, A. Bednarkiewicz, X. Liu and D. Jin, *Nat. Commun.*, 2018, **9**, 1–12.
22 Y. Zhang, X. Zhu and Y. Zhang, *ACS Nano*, 2021, **15**, 3709–3735.
23 K. Li and R. V. Deun, *Inorg. Chem.*, 2019, **58**, 6821–6831.
24 B. P. Kore, A. Kumar, L. Erasmus, R. E. Kroon, J. J. Terblans, S. J. Dhoble and H. C. Swart, *Inorg. Chem.*, 2018, **57**, 288–299.
25 M. K. Mahata, T. Koppe, K. Kumar, H. Hofsäss and U. Vetter, *Sci. Rep.*, 2020, **10**, 1–12.
26 H. Suo, C. Guo, W. Wang, T. Li, C. Duan and M. Yin, *Dalton Trans.*, 2016, **45**, 2629–2636.
27 P. Tadge, I. Martín, S. Rai, S. Sapra, T. Chen, V. Lavín, R. Yadav and S. Ray, *J. Lumin.*, 2022, **252**, 119261.
28 X. Wang, Y. Chen, F. Liu and Z. Pan, *Nat. Commun.*, 2020, **11**, 1–8.
29 G. Chen, C. Yang, B. Aghahadi, H. Liang, Y. Liu, L. Li and Z. Zhang, *J. Opt. Soc. Am. B*, 2010, **27**, 1158–1164.
30 L. Xing, W. Yang, J. Lin, M. Huang and Y. Xue, *Sci. Rep.*, 2017, **7**, 1–7.
31 X. Zhou, J. Qiao and Z. Xia, *Chem. Mater.*, 2021, **33**, 1083–1098.
32 X. Gao, W. Zhang, X. Wang, X. Huang and Z. Zhao, *J. Alloys Compd.*, 2022, **893**, 162265.
33 T. V. Gavrilović, D. J. Jovanović, L. V. Trandafilović and M. D. Dramićanin, *Opt. Mater.*, 2015, **45**, 76–81.
34 S. K. Gupta, K. Sudarshan, A. K. Yadav, R. Gupta, D. Bhattacharyya, S. N. Jha and R. M. Kadam, *Inorg. Chem.*, 2018, **57**, 821–832.
35 S. Sinha, M. K. Mahata, H. Swart, A. Kumar and K. Kumar, *New J. Chem.*, 2017, **41**, 5362–5372.
36 R. Yadav, R. Yadav, A. Bahadur and S. Rai, *RSC Adv.*, 2016, **6**, 51768–51776.
37 S. Chang, J. Fu, X. Sun, G. Bai, G. Liu, K. Wang, L. Xu, Q. Wei, T. Meier and M. Tang, *Inorg. Chem.*, 2022, **61**, 3746–3753.
38 F. Chun, B. Zhang, H. Liu, W. Deng, W. Li, M. Xie, C. Luo and W. Yang, *Dalton Trans.*, 2018, **47**, 17515–17524.
39 M. E. Foley, R. W. Meulenberg, J. R. McBride and G. F. Strouse, *Chem. Mater.*, 2015, **27**, 8362–8374.
40 R. E. Rojas-Hernandez, F. Rubio-Marcos, I. Romet, A. Del Campo, G. Gorni, I. Hussainova, J. F. Fernandez and V. Nagirnyi, *Inorg. Chem.*, 2022, **61**, 11886–11896.
41 G. N. Starostin, I. A. Zvonareva, D. A. Medvedev and S. V. Zvonarev, *Ceram. Int.*, 2022, **48**, 35606–35613.
42 Monika, R. S. Yadav, A. Bahadur and S. B. Rai, *J. Phys. Chem. C*, 2020, **124**, 10117–10128.
43 R. S. Yadav, A. Rai and S. B. Rai, *Sci. Rep.*, 2021, **11**, 1–17.
44 G. Gaikwad, N. Rohra, C. Kumar, S. Jadhav, H. D. Sarma, L. Borade, S. Chakraborty, S. Bhagwat, P. Dandekar and R. Jain, *J. Drug Delivery Sci. Technol.*, 2021, **63**, 102485.
45 S. Lohar, S. Jadhav, R. Chakravarty, S. Chakraborty, H. D. Sarma and A. Dash, *Appl. Radiat. Isot.*, 2020, **161**, 109161.
46 D. Ni, W. Bu, S. Zhang, X. Zheng, M. Li, H. Xing, Q. Xiao, Y. Liu, Y. Hua, L. Zhou, W. Peng, K. Zhao and J. Shi, *Adv. Funct. Mater.*, 2014, **24**, 6613–6620.
47 X. Jiang, Z. Zhang, T. Zhang, C. Li, Z. Leng, W. Yang, X. Wang, X. Shi, X. Zhang and H. Sha, *J. Lumin.*, 2022, **245**, 118759.
48 Q. Su, H.-L. Wei, Y. Liu, C. Chen, M. Guan, S. Wang, Y. Su, H. Wang, Z. Chen and D. Jin, *Nat. Commun.*, 2021, **12**, 4367.
49 S. Yan, Y. Liang, Y. Chen, J. Liu, D. Chen and Z. Pan, *Dalton Trans.*, 2021, **50**, 8457–8466.
50 M. Malinowski, Z. Frukacz, M. Szuflińska, A. Wnuk and M. Kaczkan, *J. Alloys Compd.*, 2000, **300**, 389–394.
51 M. Malinowski, M. Kaczkan, A. Wnuk and M. Szuflinska, *J. Lumin.*, 2004, **106**, 269–279.
52 W. Carnall, P. Fields and K. Rajnak, *J. Chem. Phys.*, 1968, **49**, 4450–4455.
53 J. Suyver, A. Aebischer, S. García-Revilla, P. Gerner and H. Güdel, *Phys. Rev. B: Condens. Matter Mater. Phys.*, 2005, **71**, 125123.
54 Y. Peng, L. Xu, J. Peng, T. Wang, Q. Wang, Y. Li, Z. Yin, J. Han, J. Qiu and Z. Yang, *J. Lumin.*, 2022, **252**, 119269.
55 A. S. Kumar, R. A. Kumar and R. Vijayakumar, *J. Mater. Sci.: Mater. Electron.*, 2022, **33**, 21297–21310.
56 S. K. Gupta, K. Sudarshan, P. S. Ghosh, A. P. Srivastava, S. Bevara, P. K. Pujari and R. M. Kadam, *J. Mater. Chem. C*, 2016, **4**, 4988–5000.
57 Z. Zhang, Y. Yang, M. Zhao, L. Lu, F. Zhang and Y. Fan, *ACS Appl. Bio Mater.*, 2022, **5**, 2935–2942.
58 K. Du, P. Lei, L. Dong, M. Zhang, X. Gao, S. Yao, J. Feng and H. Zhang, *Appl. Mater. Today*, 2020, **18**, 100497.
59 Y. Xing, L. Li, X. Ai and L. Fu, *Int. J. Nanomed.*, 2016, **11**, 4327.
60 M. Buchner, P. G. Calavia, V. Muhr, A. Kröninger, A. J. Baeumner, T. Hirsch, D. A. Russell and M. J. Marín, *Photochem. Photobiol. Sci.*, 2019, **18**, 98–109.
61 B. Chen, Y. Wang, Y. Guo, P. Shi and F. Wang, *ACS Appl. Mater. Interfaces*, 2021, **13**, 2327–2335.

62 R. Lv, D. Wang, L. Xiao, G. Chen, J. Xia and P. N. Prasad, *Sci. Rep.*, 2017, **7**, 15753.
63 M. Nahorniak, O. Pop-Georgievski, N. Velychkivska, M. Filipová, E. Rydvalová, K. Gunár, P. Matouš, U. Kostiv and D. Horák, *Life*, 2022, **12**, 1383.
64 K. Ovejero Paredes, D. Díaz-García, V. García-Almodóvar, L. Lozano Chamizo, M. Marciello, M. Díaz-Sánchez, S. Prashar, S. Gómez-Ruiz and M. Filice, *Cancers*, 2020, **12**, 187.
65 S. Chibh, K. Kaur, U. K. Gautam and J. J. Panda, *Nanoscale*, 2022, **14**, 715–735.
66 R. Chakravarty, A. Guleria, S. Jadhav, C. Kumar, A. K. Debnath, H. D. Sarma and S. Chakraborty, *Ind. Eng. Chem. Res.*, 2020, **59**, 22492–22500.